# Disproportionation of $SO_2$ at High Pressure and Temperature



Wencheng Lu,[1] Siyu Liu,[1] Guangtao Liu,[1] Kun Hao,[1] Mi Zhou,[1] Pengyue Gao,[1] Hongbo Wang,[1] Jian Lv,[1] Huiyang Gou,[2] Guochun Yang,[3] Yanchao Wang,[1,*] and Yanming Ma[1,4]

[1]*State Key Laboratory of Superhard Materials and International Center of Computational Method & Software, College of Physics, Jilin University, Changchun 130012, China*

[2]*Center for High Pressure Science and Technology Advanced Research, Beijing 100094, China*

[3]*State Key Laboratory of Metastable Materials Science and Technology and Key Laboratory for Microstructural Material Physics of Hebei Province, School of Science, Yanshan University, Qinhuangdao 066004, China*

[4]*International Center of Future Science, Jilin University, Changchun 130012, China*

(Received 22 September 2021; revised 26 December 2021; accepted 18 February 2022; published 10 March 2022)

Materials once suffered at high-pressure and high-temperature (HPHT) conditions often exhibit exotic phenomena that defy conventional wisdom. The behaviors of sulfur dioxide ($SO_2$), one of the archetypal simple molecules, at HPHT conditions have attracted a great deal of attention due to its relevance to the S cycle between deep Earth and the atmosphere. Here we report the discovery of an unexpected disproportionation of $SO_2$ via bond breaking into elemental S and sulfur trioxide ($SO_3$) at HPHT conditions through a jointly experimental and theoretical study. Measured x-ray diffraction and Raman spectroscopy data allow us to solve unambiguously the crystal structure (space group $R\bar{3}c$) of the resultant $SO_3$ phase that shows an extended framework structure formed by vertex-sharing octahedra $SO_6$. Our findings lead to a significant extension of the phase diagram of $SO_2$ and suggest that $SO_2$, despite its abundance in Earth's atmosphere and ubiquity in other giant planets, is not a stable compound at HPHT conditions relevant to planetary interiors, providing important implications for elucidating the S chemistry in deep Earth and other giant planets.

DOI: 10.1103/PhysRevLett.128.106001

For simple molecules (e.g., $O_2$, $H_2S$, $CO_2$, $NO_2$, $H_2O$, $NH_3$, and $CH_4$), a plethora of complex phenomena such as structural phase transitions, amorphization, dissociation, metallization, and superconductivity can appear at high-pressure and high-temperature (HPHT) conditions [1]. Among them, pressure-induced phase transitions are most common by accompanying the formation of a variety of crystal structures that are not accessible at ambient conditions. Compressed molecular solids are often known to acquire extended solids with strong covalent-bonding frameworks and ultimately transform into ionic phases (e.g., $CO_2$, $H_2O$, $NO_2$, and $NH_3$) [2–11]. On the other hand, unexpected chemical disproportionation reactions have been observed for certain simple molecules (e.g., CO, $CH_4$, NO, and $H_2S$) [12–19], producing materials that sometimes adopt exotic superconducting property [20].

As one of the typical simple molecules, $SO_2$ is considered as an archetypal system. Its $p$ bond and hybridization properties can be severely affected by HPHT conditions. Knowledge of these behaviors is vital for understanding S—O bonding and the structural evolutions of simple molecules. In addition, $SO_2$ is an important atmospheric molecule on Earth and outer planets such as Venus [21] and the Jovian moon Io [22–24], which is produced through volcanic eruptions [25]. As a result, $SO_2$ is expected to be constituent of the planetary interiors [26].

At ambient pressure, $SO_2$ crystallizes into an orthorhombic $Aba2$ structure having four molecules per unit cell at 143 K [27]. Two high-pressure molecular phases ($SO_2$-II and $SO_2$-III) have been observed at pressures up to 7.5 GPa [28]. Upon further compression, a phase transition into an extended solid of $SO_2$-IV has been observed at 17.5 GPa [29]. Unfortunately, since there is absence of x-ray diffraction (XRD) data, the crystal structures of these high-pressure phases ($SO_2$-II, $SO_2$-III, and $SO_2$-IV) are not known. Very recently, a pressure-induced phase transition in the amorphous solid from a molecular to a polymeric phase was reported at 26 GPa [30]. Overall, the previous studies of $SO_2$ are mainly performed at a relatively low-pressure and low-temperature regime (below 60 GPa and room temperature), while the stability range and nature of $SO_2$ at HPHT conditions remain largely unknown. There is a fundamental interest for the study at HPHT conditions relevant to planetary interiors since $SO_2$ is expected to play a pertinent role in the understanding of the S cycle between the atmosphere and deep Earth.

Here we have carried out *ab initio* calculations and HPHT experiments to establish the phase diagram of compressed $SO_2$ solids. Unexpectedly, a chemical disproportionation

 

reaction of $SO_2$ was discovered at 95.2 GPa and 2700 K, where $SO_2$ decomposes into the elemental S and sulfur trioxide $SO_3$. The crystal structure of the resultant high-pressure phase of $SO_3$ was determined to have a hexagonal $R\bar{3}c$ structure via *in situ* synchrotron XRD and Raman measurements, which is in excellent agreement with our theoretical prediction. Our discovery has renewed the fundamental principles that govern the chemistry of $SO_2$ under extreme conditions and substantially extended the phase diagram of $SO_2$ to HPHT conditions relevant to planetary interiors.

Our *ab initio* calculations were performed using density-functional theory with the Perdew-Burke-Ernzerh generalized gradient approximation [31], as implemented in the VASP code [32]. The plane wave basis set cutoff energy of 900 eV and Monkhorst-Pack [33] Brillouin zone sampling grid of $2\pi \times 0.03$ Å$^{-1}$ were used to ensure enthalpy convergence of better than 1 meV/atom. Our calculations reveal the phase transitions sequence of $Aba2 \rightarrow Pna2_1 \rightarrow Pmc2_1$ [30] at low pressure and 0 K. The $Pna2_1$ structure is a molecular crystal [Fig. 1(a)], whereas the $Pmc2_1$ structure is a polymeric phase containing a chain formed by the vertex-sharing $SO_3$ pyramids [Fig. 1(b)]. Note that the $Pna2_1$ can be viewed as an intermediate structure between molecular and polymeric crystals, which is stable at 1.5–15.5 GPa [see Supplemental Material, Fig. S10(b) [34]]. Upon further compression to 65 GPa, $SO_2$ becomes thermodynamically unstable with respect to the dissociation into elemental S and $SO_3$ via the reaction route of $3SO_2 \rightarrow S + 2SO_3$. The hexagonal $R\bar{3}c$ structure of $SO_3$ predicted in an earlier work [35] and our CALYPSO [36–38] structure-searching simulation [39] is more stable than the ambient-pressure $\alpha$ phase of $SO_3$ at the pressure of 72 GPa. Unlike the known $\alpha$ phase of $SO_3$ having the partially polymerized chain structure, $R\bar{3}c$-$SO_3$ is fully polymerized into a covalent structure composed of the vertex-sharing $SO_6$ octahedra, where S atoms are considered as being $sp^3$-type hybridization [Fig. 1(c)]. The dynamic stabilities of the predicted structures of $Pna2_1$-$SO_2$, $Pmc2_1$-$SO_2$, and $R\bar{3}c$-$SO_3$ were examined by the phonon spectrum calculations through the finite displacement method as implemented in the PHONOPY code [40]. No imaginary frequencies of the phonon dispersions for these structures (Fig. S2 [34]) were found, indicating they are dynamically stable. For further details on the calculations, see Supplemental Material and Refs. [41–45].

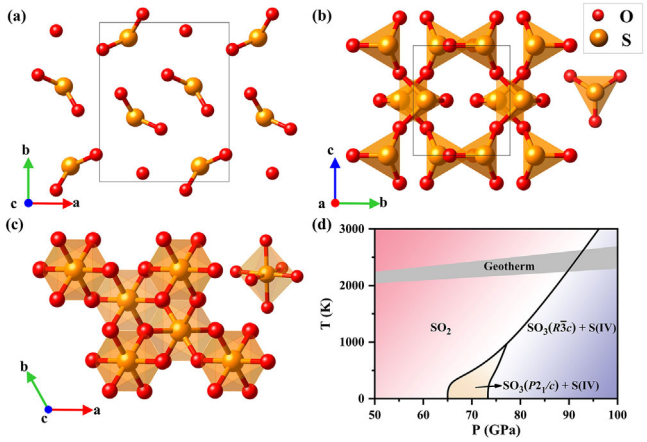


FIG. 1. The predicted crystal structures of (a) $Pna2_1$-$SO_2$, (b) $Pmc2_1$-$SO_2$, and (c) $R\bar{3}c$-$SO_3$ (c). (d) Thermodynamic phase diagram of $SO_2$ determined using first-principles density-functional theory. The gray region presents the geotherm of Earth from Ref. [46].

In order to provide more information from a theory ground to aid for subsequent experimental synthesis, we further examine vibrational contributions and entropic effects for the relevant phases and construct the finite-temperature phase diagram of $SO_2$ using the quasiharmonic approximation [Fig. 1(d)]. It is found that the estimated differences of zero-point energy between the reactants ($SO_2$) and products ($R\bar{3}c$-$SO_3$, S-IV) are about 0.104 and 0.106 eV/f.u. at 70 and 80 GPa, respectively, giving a rather small modification on the threshold pressure from 72 to 74 GPa for the disproportionation reaction of $SO_2$ into S and $R\bar{3}c$-$SO_3$ at 0 K. However, the threshold pressure is largely revised by the inclusion of the temperature effect, and it goes from 65 GPa at 0 K to 88 GPa at 2000 K.

The decomposition of compressed $SO_2$ is driven by the denser structure packing in $SO_3$ and S solids. Our calculations show that the decomposition at 74 GPa accepts volumes of 6.27 Å$^3$/atom for $SO_3$ in the $R\bar{3}c$ structure, 10.76 Å$^3$/atom for the S-IV phase, and 7.70 Å$^3$/atom for $SO_2$, with a large volume shrinkage of $\Delta V/V = -12.12\%$ associated with a higher packing efficiency (see Supplemental Material, Fig. S3 [34]). Consequently, the pressure-volume term in Gibbs free energy strongly favors the decomposition of $SO_2$ at high pressure. In addition, the decomposition of $SO_2$ seems to be intimately tied to multivalent element speciation of S, whose oxidation states are changed from +4 to a mixture of 0 and +6 via self-redox reaction under compressions.

The *in situ* Raman spectra of $SO_2$ over a broad pressure were investigated at room temperature [Fig. 2(a)]. As pressure increases, the observed low-frequency modes ($60 - 360$ cm$^{-1}$) shift to the higher wave number region and two new bands located at 515 and 653 cm$^{-1}$ appear at 21.2 GPa. Under further compression, this phase transition continues as evidenced by the intensity enhancement of the newly observed modes around 522 and 658 cm$^{-1}$, and the lattice modes and the high-frequency peaks at 1166 and 1234 cm$^{-1}$ weaken gradually and disappear completely when the pressure approaches 31.6 GPa. The peak positions and pressure-induced changes in Raman frequencies of $SO_2$ at room temperature plotted in Fig. 2(b) show an excellent agreement with earlier experimental data (see

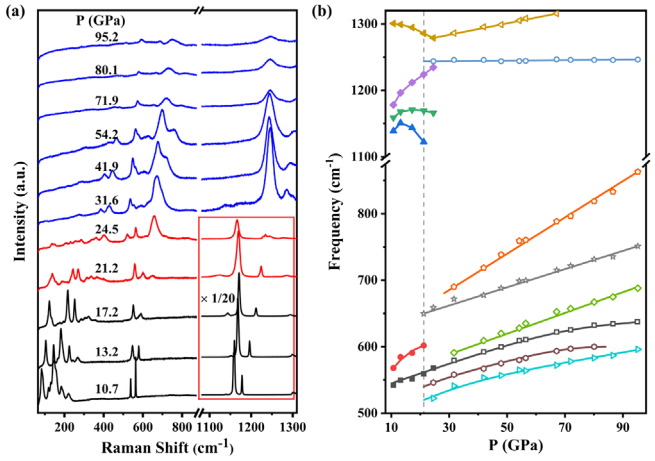


FIG. 2. Raman spectra of $SO_2$ solid upon compression to 95.2 GPa at room temperature. (a) Selected high-pressure Raman spectra of solid $SO_2$ measured with exciting wavelength of 633 nm. (b) Pressure dependence of Raman shifts. Different symbols denote different Raman peaks.

Supplemental Material, Fig. S4 [34]). It is observed that the phase transition from molecular $SO_2$-III to the extended solid of $SO_2$-IV phase occurs at nearly 21.2 GPa and room temperature [29]. The obtained transition is supported by our *ab initio* prediction, where a $Pmc2_1$ structure is calculated to be energetically more favorable than the $Pna2_1$ structure above 15.5 GPa. Direct comparison of the calculated vibrational modes and experimental Raman spectrum obtained at 54.2 GPa (see Fig. S5 [34]) indicates that $Pmc2_1$-$SO_2$ is a good candidate structure for the polymeric phase of $SO_2$-IV. Upon further compression, the linewidth of the peaks increases, but the Raman profiles exhibit no qualitative changes except that the 546 cm$^{-1}$ band gradually weakens and indistinguishably merges into the 522 cm$^{-1}$ mode around 86 GPa. It is inferred that no obvious phase transition takes place over the pressure range from 21.2 to 95.2 GPa at room temperature.

When there is an expectation on the disproportionation associated with bonds breaking, a large activation barrier is often needed to be overcome by the use of high temperatures in order to seek the alternative thermodynamic stable phase (e.g., CO [47], NO [18], and $H_2S$ [14]). Also, guided by our theory in Fig. 1(d), we have performed HPHT experiments on $SO_2$ by employing an off-line laser-heating technique in a diamond anvil cell. High-purity $SO_2$ (99.9%) was loaded into a sample chamber by means of cryogenic loading. The samples were compressed to 95.2 GPa and heated up to a temperature of approximately 2700 K with an off-line pulsed Nd:YAG laser (a wavelength of 1064 nm) system. The heating process of $SO_2$ was accomplished by the continuously slow movement of a 10 m laser spot on the samples, and the total heating time per experimental run was about 1 min. We find via a near-infrared transmittance spectrum measurement that $SO_2$ samples absorb the Nd:YAG laser in an efficient way at high pressure (see Supplemental Material, Fig. S6 [34]). For further details on the experimental methods see Supplemental Material and Refs. [48–51].

The Raman spectra in a domain of frequencies from 250 to 1300 cm$^{-1}$ collected before and after laser heating were shown in Fig. 3(a), together with the Raman active modes predicted in $R\bar{3}c$-$SO_3$. It is seen that all the original Raman peaks of $SO_2$ disappear and six distinct peaks are present after laser heating. The observed low-frequency modes (285, 356, 406, and 485 cm$^{-1}$) are in good agreement with those of S (phase IV) after laser heating at 92.8 GPa. A group theory analysis shows that there are four Raman

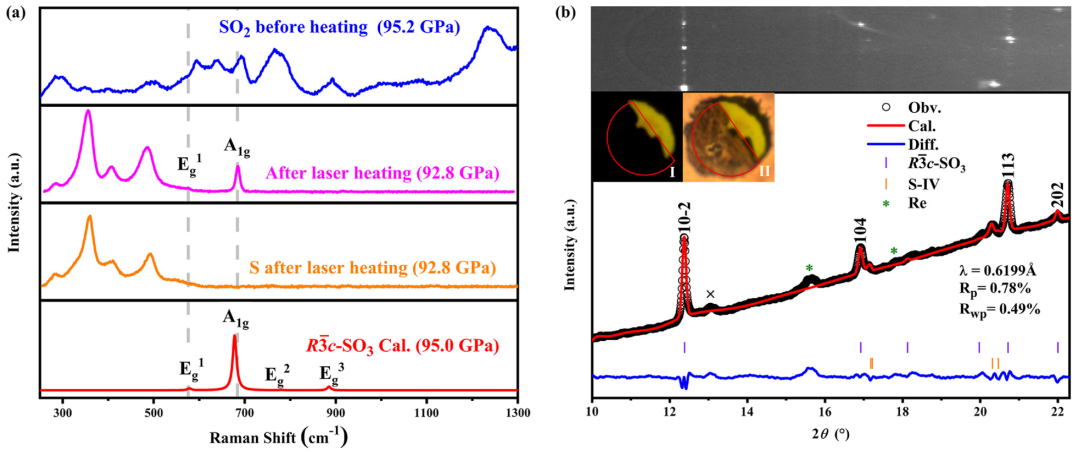


FIG. 3. (a) Raman spectra for $SO_2$ before and after laser heating, and elemental *S* after heating measured with exciting wavelength of 633 nm, as well as that obtained by simulation of refined structure of $R\bar{3}c$-$SO_3$. (b) Measured XRD patterns at 95 GPa and calculated Bragg peaks of $R\bar{3}c$-$SO_3$ and S-IV phases. The x-ray wavelength is 0.6199 Å. The photographs of the sample taken after laser heating under combined transmitted (inset I) and reflected (inset II) illumination. The transparent area is the sample morphology before heating. The regions marked by a red circle are the sample morphology after heating. For a direct comparison of the changes of the samples before and after heating, only half of the samples were heated, and the other half remained cool.

active modes ($\Gamma = 3E_g + A_{1g}$) for $R\bar{3}c$-$SO_3$. Two modes with frequencies of 576 and 684 $cm^{-1}$ are consistent with $E_g^1$ and $A_{1g}$ modes predicted in the $R\bar{3}c$-$SO_3$ phase; however, the other two Raman modes of $E_g^2$ and $E_g^3$ are too weak to be observed. Furthermore, the Raman spectra during decompression of the samples were shown in the Supplemental Material (Fig. S7) [34]. The characteristic $A_{1g}$ mode of $R\bar{3}c$-$SO_3$ phase becomes weaker in intensity with decreasing pressure and clearly persists to 67.2 GPa (see Fig. S7 [34]), a threshold pressure for the metastability of $R\bar{3}c$-$SO_3$.

In order to further confirm the $R\bar{3}c$-$SO_3$ structure of the heated samples, the powder XRD patterns obtained from a synchrotron radiation experiment were collected at 95 GPa and shown in Fig. 3(b). New diffraction peaks do not correspond to any $SO_2$ solids. The Rietveld refinements of the diffraction patterns confirm that these new peaks correspond to S-IV [52] and $R\bar{3}c$-$SO_3$ phases, respectively. More specifically, the observed peaks at 12.38°, 16.94°, 20.73°, and 21.99° match well with the $(1\,0\,-2)$, $(1\,0\,4)$, $(1\,1\,3)$, and $(2\,0\,2)$ crystal planes of $R\bar{3}c$-$SO_3$, respectively. The obtained lattice parameters of $R\bar{3}c$-$SO_3$ at 95 GPa, $a = b = 3.93$ Å, and $c = 10.71$ Å, are close to theoretical data of $a = b = 3.94$ and $c = 10.74$ Å. Note that the XRD patterns of the heated samples exhibit a nonindexed peak marked by "×". Because of the "broad" feature of this peak (see Supplemental Material, Fig. S8 [34]), we speculate that it might be derived from a residue of the amorphous phase of $SO_2$ [30].

Moreover, the sample has undergone a significant color change from transparency to opaque with a metallic luster after heating [insets of Fig. 3(b)] and the metallic nature may be relevant to the decomposed product of metallic S-IV. The presence of elemental S and $SO_3$ manifested in the measured XRD data provides a solid confirmation for the decomposition of compressed $SO_2$ into S-IV and $R\bar{3}c$-$SO_3$ as predicted in our calculations [39].

It is known that $SO_2$ can react with various metals (e.g., Fe [53], Co [54], and Ni [55]) at high temperatures. Considering that no peaks for Re-containing compounds exhibit in the measured XRD patterns of the heated samples, the chemical reaction between Re gasket and $SO_2$ can be safely excluded in our experiments. Furthermore, we have also performed a laser-heating experiment by using Au as an inner gasket to avoid the direct contact between Re and $SO_2$ (see Supplemental Material, Fig. S9 [34]). After laser heating, the resultant Raman spectrum of the samples is identical to the one obtained without the inner gasket of Au, giving strong support for the fact that the decomposition of $SO_2$ takes place no matter whether the samples are in contact with the Re gasket.

We have examined electronic band structures and density of states to decipher the electronic properties of $R\bar{3}c$-$SO_3$ [Fig. 4(a)]. The results reveal that the $R\bar{3}c$-$SO_3$ is an insulator with a large band gap of 3.6 eV at 70 GPa and a continuous widening of band gaps is predicted from 3.6 to 4.2 eV at pressures ranging from 70 to 100 GPa [see Supplemental Material, Fig. S10(a) [34] ]. This anomalous behavior of pressure-promoted band gap may be attributed to the enhanced ionicity of $R\bar{3}c$-$SO_3$ as evidenced by more charge transfer from S to O with increasing pressures [Fig. S10(b) [34] ].

It has long been known that the exchange of S between the surface and deep Earth, i.e., transporting S to the mantle via subduction and returning it to the surface by volcanic degassing, results in a deep global S cycle [26]. Previous studies suggest that the sulfate minerals of $MSO_4$ ($M$ = Ca, Mg, and Fe) [56,57] and $Fe_2(SO_4)_3$ [58] as important carriers can transport S from the surface to deep Earth by the subducting slabs [59,60], while S returns to the surface by volcanic degassing in the form of S-bearing gases (e.g., $SO_2$ and $SO_3$) [61–64]. It has been demonstrated that the volcanic degassing of $SO_2$ originates from the redox reactions of S-bearing minerals (e.g., $MgSO_4$ and $CaSO_4$) [25,39]. However, the source of $SO_3$, released during volcanic eruptions, remains poorly understood.

Given that the decomposition of the sulfates may be a viable route for production of $SO_3$, we thus explore the possibility of the decompositions of the subducted sulfates

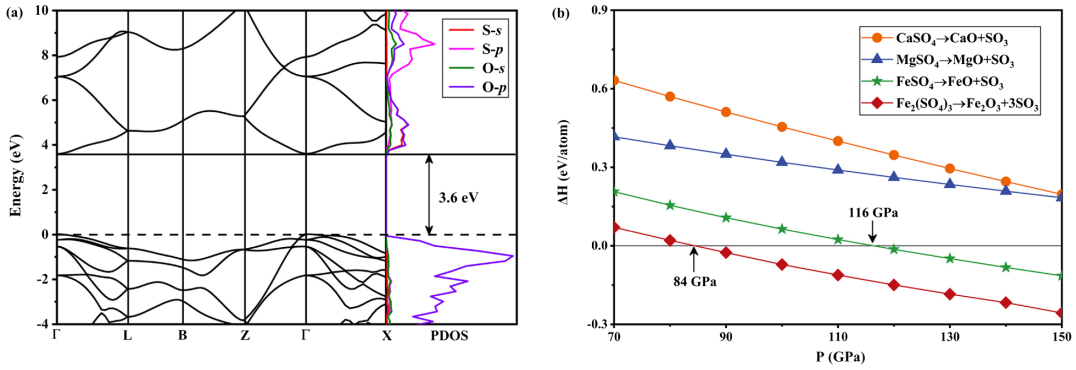


FIG. 4. (a) Band structures (left) and partial density of states (right) of $R\bar{3}c$-$SO_3$ at 70 GPa. (b) Relative enthalpies for sulfates to decompose into $SO_3$ and pertinent oxides at high pressure.

of $MSO_4$ ($M$ = Ca, Mg, and Fe) and $Fe_2(SO_4)_3$ with respect to oxides (e.g., CaO, MgO, FeO, $FeO_2$, and $Fe_2O_3$) abundant within Earth's mantle and $SO_3$ as products. (For details on the calculations, see Supplemental Material and Refs. [65–74]). We find that, unlike $MgSO_4$ and $CaSO_4$, decomposition reactions of $FeSO_4$ and $Fe_2(SO_4)_3$ indeed occur at 84 and 116 GPa, respectively, corresponding to pressure conditions at deep Earth's mantle [Fig. 4(b)]. In sharp contrast to the mechanism for production of $SO_2$ via redox reactions with varied oxidation states of S, the decomposition of subducted sulfates to produce $SO_3$ does not involve any changes in oxidation states of S. These findings reveal that the volcanic degassing of $SO_3$ might be arising from the decompositions of $FeSO_4$ and $Fe_2(SO_4)_3$. The production of $SO_3$ by decomposition of subducted sulfates offers insights for understanding deep Earth chemical reactions relevant to S cycles inside our planet and implies that $SO_3$, which was not previously considered, should be taken into account for the construction of a realistic model of Earth's mantle.

The pressure homology rule states that light elements behave at high pressure, like those in heavier elements from the same group of the periodic table at lower pressures [75]. For the heavier elements oxides in the VIA group, $SeO_2$ has a partially polymerized chain structure at pressure up to 20 GPa [76,77], while $TeO_2$ adopts a fully polymerized covalent structure even at ambient pressure [78,79]. There is an expectation that $SO_2$ might also have a polymerized structure at high pressures, in resemblance to those in $SeO_2$ and $TeO_2$. In contrast to these expectations, our findings unravel the occurrence of an unexpected disproportionation reaction of $SO_2$ into $SO_3$ and elemental S at high pressure.

In summary, we provided theoretical and experimental evidence for the occurrence of a chemical disproportionation reaction of $SO_2$ at HPHT conditions, where $SO_2$ was proven to decompose into the known S-IV phase and a newly established polymeric $R\bar{3}c$ phase of $SO_3$. The resulting phase of $SO_3$ contains vertex-sharing octahedra $SO_6$ units and exhibits an anomalous behavior of pressure-enhanced band gap. The occurrence of decomposition of compressed $SO_2$ is originated from the volume reduction favorable for a denser structure packing. These findings enrich fundamental behaviors of compressed simple molecules and create an extended phase diagram of $SO_2$ at HPHT conditions relevant to planetary interiors, thereby offering important implications for the deep S cycle within Earth's mantle and elucidating the S chemistry of planetary interiors.

We thank B.L. for constructive discussions. This paper is dedicated to the 70th anniversary of the physics of Jilin University.

This research was supported by the National Natural Science Foundation of China under Grants No. 11404128, No. 11822404, No. 11534003, No. 12174142, No. 11774127, No. 12034009, 91961204, No. 12074139, and No. 21873017, the Program for JLU Science and Technology Innovative Research Team, and the Science Challenge Project, No. TZ2016001. Part of the calculation was performed in the high-performance computing center of Jilin University. The XRD measurements were supported by BL15U1 at Shanghai Synchrotron Radiation Facility and BL4W2 at Beijing Synchrotron Radiation Facility.

W. L., S. L., and G. L. contributed equally to this work.

*wyc@calypso.cn

[1] Russell J. Hemley, Effects of high pressure on molecules, Annu. Rev. Phys. Chem. **51**, 763 (2000).
[2] Cheng Lu, Maosheng Miao, and Yanming Ma, Structural evolution of carbon dioxide under high pressure, J. Am. Chem. Soc. **135**, 14167 (2013).
[3] V. Iota, C. S. Yoo, and H. Cynn, Quartzlike carbon dioxide: An optically nonlinear extended solid at high pressures and temperatures, Science **283**, 1510 (1999).
[4] Mario Santoro, Jung-Fu Lin, Ho-Kwang Mao, and Russell J. Hemley, In situ high Pt raman spectroscopy and laser heating of carbon dioxide, J. Chem. Phys. **121**, 2780 (2004).
[5] Mario Santoro, Federico A. Gorelli, Roberto Bini, Giancarlo Ruocco, Sandro Scandolo, and Wilson A. Crichton, Amorphous silica-like carbon dioxide, Nature (London) **441**, 857 (2006).
[6] C. S. Yoo, H. Cynn, F. Gygi, G. Galli, V. Iota, M. Nicol, S. Carlson, D. Häusermann, and C. Mailhiot, Crystal Structure of Carbon Dioxide at High Pressure: "Superhard" Polymeric Carbon Dioxide, Phys. Rev. Lett. **83**, 5527 (1999).
[7] Valentin Iota, Choong-Shik Yoo, Jae-Hyun Klepeis, Zsolt Jenei, William Evans, and Hyunchae Cynn, Six-fold coordinated carbon dioxide VI, Nat. Mater. **6**, 34 (2007).
[8] A. F. Goncharov, V. V. Struzhkin, M. S. Somayazulu, R. J. Hemley, and Ho-Kwang Mao, Compression of ice to 210 Gigapascals: Infrared evidence for a symmetric hydrogen-bonded phase, Science **273**, 218 (1996).
[9] S. F. Agnew, B. I. Swanson, L. H. Jones, R. L. Mills, and D. Schiferl, Chemistry of nitrogen oxide ($N_2O_4$) at high pressure: Observation of a reversible transformation between molecular and ionic crystalline forms, J. Phys. Chem. **87**, 5065 (1983).
[10] Chris J. Pickard and R. J. Needs, Highly compressed ammonia forms an ionic crystal, Nat. Mater. **7**, 775 (2008).
[11] S. Ninet, F. Datchi, P. Dumas, M. Mezouar, G. Garbarino, A. Mafety, C. J. Pickard, R. J. Needs, and A. M. Saitta, Experimental and theoretical evidence for an ionic crystal of ammonia at high pressure, Phys. Rev. B **89**, 174103 (2014).
[12] Jian Sun, Dennis D. Klug, Chris J. Pickard, and Richard J. Needs, Controlling the Bonding and Band Gaps of Solid Carbon Monoxide with Pressure, Phys. Rev. Lett. **106**, 145502 (2011).
[13] Guoying Gao, Artem R. Oganov, Yanming Ma, Hui Wang, Peifang Li, Yinwei Li, Toshiaki Iitaka, and Guangtian Zou, Dissociation of methane under high pressure, J. Chem. Phys. **133**, 144508 (2010).

[14] Mari Einaga, Masafumi Sakata, Takahiro Ishikawa, Katsuya Shimizu, Mikhail I. Eremets, Alexander P. Drozdov, Ivan A. Troyan, Naohisa Hirao, and Yasuo Ohishi, Crystal structure of the superconducting phase of sulfur hydride, Nat. Phys. **12**, 835 (2016).
[15] W. J. Evans, M. J. Lipp, C.-S. Yoo, H. Cynn, J. L. Herberg, R. S. Maxwell, and M. F. Nicol, Pressure-induced polymerization of carbon monoxide: Disproportionation and synthesis of an energetic lactonic polymer, Chem. Mater. **18**, 2520 (2006).
[16] Allen I. Katz, David Schiferl, and Robert L. Mills, New phases and chemical reactions in solid carbon monoxide under pressure, J. Phys. Chem. **88**, 3176 (1984).
[17] R. L. Mills, D. Schiferl, A. I. Katz, and B. W. Olinger, New phases and chemical reactions in solid CO under pressure, J Phys. Colloq. **45**, C8 (1984).
[18] Stephan F. Agnew, B. I. Swanson, L. H. Jones, and R. L. Mills, Disproportionation of nitric oxide at high pressure, J. Phys. Chem. **89**, 1678 (1985).
[19] Maddury Somayazulu, Achintya Madduri, Alexander F. Goncharov, Oliver Tschauner, Paul F. McMillan, Ho-Kwang Mao, and Russell J. Hemley, Novel Broken Symmetry Phase from $N_2O$ at High Pressures and High Temperatures, Phys. Rev. Lett. **87**, 135504 (2001).
[20] A. P. Drozdov, M. I. Eremets, I. A. Troyan, Vadim Ksenofontov, and Sergii I. Shylin, Conventional superconductivity at 203 kelvin at high pressures in the sulfur hydride system, Nature (London) **525**, 73 (2015).
[21] W. J. Markiewicz, D. V. Titov, S. S. Limaye, Horst Uwe Keller, Nikoley Ignatiev, Ralf Jaumann, Nicolas Thomas, Harald Michalik, Richard Moissl, and P. Russo, Morphology and dynamics of the upper cloud layer of Venus, Nature (London) **450**, 633 (2007).
[22] B. A. Smith, E. M. Shoemaker, S. W. Kieffer, and A. F. Cook, The role of SO2 in volcanism on Io, Nature (London) **280**, 738 (1979).
[23] Rosaly M. C. Lopes and David A. Williams, Io after Galileo, Rep. Prog. Phys. **68**, 303 (2005).
[24] Robert M.. Nelson and William D Smythe, Spectral reflectance of solid sulfur trioxide (0.25–5.2 $\mu$m): Implications for Jupiter's satellite Io, Icarus **66**, 181 (1986).
[25] Victor Kress, Magma mixing as a source for pinatubo sulphur, Nature (London) **389**, 591 (1997).
[26] Ji-Lei Li, Esther M. Schwarzenbach, Timm John, Jay J. Ague, Fang Huang, Jun Gao, Reiner Klemd, Martin J. Whitehouse, and Xin-Shui Wang, Uncovering and quantifying the subduction zone sulfur cycle from the slab perspective, Nat. Commun. **11**, 514 (2020).
[27] B. Post, R. S. Schwartz, and I. Fankuchen, The crystal structure of sulfur dioxide, Acta Crystallogr. **5**, 372 (1952).
[28] Basil I. Swanson, Lucia M. Babcock, David Schiferl, David C. Moody, Robert L. Mills, and Robert R. Ryan, Raman study of $SO_2$ at high pressure: Aggregation, phase transformations, and photochemistry, Chem. Phys. Lett. **91**, 393 (1982).
[29] Yang Song, Zhenxian Liu, Ho-Kwang Mao, Russell J. Hemley, and Dudley R. Herschbach, High-pressure vibrational spectroscopy of sulfur dioxide, J. Chem. Phys. **122**, 174511 (2005).
[30] Huichao Zhang, Ondrej Tóth, Xiao-Di Liu, Roberto Bini, Eugene Gregoryanz, Philip Dalladay-Simpson, Simone De Panfilis, Mario Santoro, Federico Aiace Gorelli, and Roman Martoňák, Pressure-induced amorphization and existence of molecular and polymeric amorphous forms in dense $SO_2$, Proc. Natl. Acad. Sci. U.S.A. **117**, 8736 (2020).
[31] John P. Perdew, Kieron Burke, and Matthias Ernzerhof, Generalized Gradient Approximation Made Simple, Phys. Rev. Lett. **77**, 3865 (1996).
[32] Georg Kresse and Jürgen Furthmüller, Efficient iterative schemes for ab initio total-energy calculations using a plane-wave basis set, Phys. Rev. B **54**, 11169 (1996).
[33] Hendrik J. Monkhorst and James D. Pack, Special points for Brillouin-zone integrations, Phys. Rev. B **13**, 5188 (1976).
[34] See Supplemental Material at http://link.aps.org/supplemental/10.1103/PhysRevLett.128.106001 for detailed descriptions of computational and experimental methods, enthalpy calculations, dynamic stabilities, volume shrinkage, electronic band structures, Raman spectra, and NIR transmittance spectra.
[35] Toomas Tamm and Pekka Pyykkö, Possible high-pressure structures of sulfur trioxide, Chem. Commun. **2002**, 336 (2002).
[36] Yanchao Wang, Jian Lv, Li Zhu, and Yanming Ma, CALYPSO: A method for crystal structure prediction, Comput. Phys. Commun. **183**, 2063 (2012).
[37] Yanchao Wang, Jian Lv, Li Zhu, and Yanming Ma, Crystal structure prediction via particle-swarm optimization, Phys. Rev. B **82**, 094116 (2010).
[38] Bo Gao, Pengyue Gao, Shaohua Lu, Jian Lv, Yanchao Wang, and Yanming Ma, Interface structure prediction via CALYPSO method, Sci. Bull. **64**, 301 (2019).
[39] Siyu Liu, Pengyue Gao, Andreas Hermann, Guochun Yang, Jian Lv, Yanming Ma, Ho-Kwang Mao, and Yanchao Wang, Stabilization of $S_3O_4$ at high pressure-implications for the sulfur excess paradox, arXiv:2109.08891.
[40] Atsushi Togo, Fumiyasu Oba, and Isao Tanaka, First-principles calculations of the ferroelastic transition between rutile-type and $CaCl_2$-type $SiO_2$ at high pressures, Phys. Rev. B **78**, 134106 (2008).
[41] P. E. Blöchl, Projector augmented-wave method, Phys. Rev. B **50**, 17953 (1994).
[42] Richard F. W. Bader, A quantum theory of molecular structure and its applications, Chem. Rev. **91**, 893 (1991).
[43] Koichi Momma and Fujio Izumi, Vesta 3 for three-dimensional visualization of crystal, volumetric and morphology data, J. Appl. Crystallogr. **44**, 1272 (2011).
[44] S. L. Dudarev, G. A. Botton, S. Y. Savrasov, C. J. Humphreys, and A. P. Sutton, Electron-energy-loss spectra and the structural stability of nickel oxide: An LSDA + U study, Phys. Rev. B **57**, 1505 (1998).
[45] Bo Gyu Jang, Duck Young Kim, and Ji Hoon Shim, Metal-insulator transition and the role of electron correlation in $FeO_2$, Phys. Rev. B **95**, 075144 (2017).
[46] Tomoo Katsura, Akira Yoneda, Daisuke Yamazaki, Takashi Yoshino, and Eiji Ito, Adiabatic temperature profile in the mantle, Phys. Earth Planet. Inter. **183**, 212 (2010).
[47] Stephane Bernard, Guido L. Chiarotti, Sandro Scandolo, and Erio Tosatti, Decomposition and Polymerization of Solid Carbon Monoxide under Pressure, Phys. Rev. Lett. **81**, 2092 (1998).

[48] Yuichi Akahama and Haruki Kawamura, Pressure calibration of diamond anvil Raman gauge to 410 GPa, J. Phys. Conf. Ser. **215**, 012195 (2010).
[49] Clemens Prescher and Vitali B. Prakapenka, DIOPTAS: A program for reduction of two-dimensional x-ray diffraction data and data exploration, High Press. Res. **35**, 223 (2015).
[50] Brian H. Toby, Expgui, a graphical user interface for gsas, J. Appl. Crystallogr. **34**, 210 (2001).
[51] Richard C. Pinkerton, Beer's law without calculus, J. Chem. Educ. **41**, 366 (1964).
[52] O. Degtyareva, M. V. Magnitskaya, J. Kohanoff, G. Profeta, S. Scandolo, M. Hanfland, M. I. McMahon, and E. Gregoryanz, Competition of Charge-Density Waves and Superconductivity in Sulfur, Phys. Rev. Lett. **99**, 155505 (2007).
[53] B. Chatterjee and A. J. Dowell, High temperature reaction of Fe in $SO_2$, Corros. Sci. **15**, 639 (1975).
[54] Kjell Holthe and Per Kofstad, High temperature corrosion of cobalt in $SO_2$, Corros. Sci. **20**, 919 (1980).
[55] Marion Seiersten and Per Kofstad, The high temperature corrosion of nickel in $SO_2$ at $500 - 800\,°C$, Corros. Sci. **22**, 487 (1982).
[56] Sébastien Jégo and Rajdeep Dasgupta, The fate of sulfur during fluid-present melting of subducting basaltic crust at variable oxygen fugacity, J. Petrol. **55**, 1019 (2014).
[57] Sandro Jahn and Christian Schmidt, Speciation in aqueous $MgSO_4$ fluids at high pressures and high temperatures from ab initio molecular dynamics and Raman spectroscopy, J. Phys. Chem. B **114**, 15565 (2010).
[58] B. Debret, M.-A. Millet, M.-L. Pons, P. Bouilhol, E. Inglis, and H. Williams, Isotopic evidence for iron mobility during subduction, Geology **44**, 215 (2016).
[59] Marie-Laure Pons, Baptiste Debret, Pierre Bouilhol, Adélie Delacour, and Helen Williams, Zinc isotope evidence for sulfate-rich fluid transfer across subduction zones, Nat. Commun. **7**, 13794 (2016).
[60] Jesse B. Walters, Alicia M. Cruz-Uribe, and Horst R. Marschall, Isotopic compositions of sulfides in exhumed high-pressure terranes: Implications for sulfur cycling in subduction zones, Geochem. Geophys. Geosyst. **20**, 3347 (2019).
[61] James Farquhar, Huiming Bao, and Mark Thiemens, Atmospheric influence of Earth's earliest sulfur cycle, Science **289**, 756 (2000).
[62] Akira Imai, Metallogenesis of porphyry Cu deposits of the Western Luzon Arc, Philippines: K-Ar ages, $SO_3$ contents of microphenocrystic apatite and significance of intrusive rocks, Resource Geol. **52**, 147 (2002).
[63] T. M. Gerlach, Evaluation of volcanic gas analyses from Kilauea volcano, J. Volcanol. Geotherm. Res. **7**, 295 (1980).
[64] Thomas Augustus Jaggar, Magmatic gases, Am. J. Sci. **238**, 313 (1940).
[65] Lourdes Gracia, Armando Beltran, Daniel Errandonea, and Juan Andres, $CaSO_4$ and its pressure-induced phase transitions. A density functional theory study, Inorg. Chem. **51**, 1751 (2012).
[66] A. Jemmy Cinthia, G. Sudha Priyanga, R. Rajeswarapalanichamy, and K. Iyakutti, Structural, electronic and mechanical properties of alkaline earth metal oxides MO (M = Be, Mg, Ca, Sr, Ba), J. Phys. Chem. Solids **79**, 23–42 (2015).
[67] A Benmakhlouf, D Errandonea, M Bouchenafa, S Maabed, A Bouhemadou, and A Bentabet, New pressure-induced polymorphic transitions of anhydrous magnesium sulfate, Dalton Trans. **46**, 5058 (2017).
[68] Qiang Zhu, Artem R. Oganov, and Andriy O. Lyakhov, Novel stable compounds in the Mg–O system under high pressure, Phys. Chem. Chem. Phys. **15**, 7696 (2013).
[69] Matthias Weil, The high-temperature $\beta$ modification of iron (ii) sulfate, Acta Crystallogr. Sect. E **63**, i192 (2007).
[70] Taedaehyeong Eom, Hyung-Kyu Lim, William A. Goddard III, and Hyungjun Kim, First-principles study of iron oxide polytypes: Comparison of GGA + $U$ and hybrid functional method, J. Phys. Chem. C **119**, 556 (2015).
[71] P. J. Rentzeperis and P. C. Christidis, The crystal structure of rhombohedral $Fe_2(SO_4)3$, Z. Kristallogr. Cryst. Mater. **144**, 341 (1976).
[72] Elena Bykova, Leonid Dubrovinsky, Natalia Dubrovinskaia, Maxim Bykov, Catherine McCammon, Sergey V. Ovsyannikov, H.-P. Liermann, Ilya Kupenko, Aleksandr I. Chumakov, Rudolf Rüffer *et al.*, Structural complexity of simple $Fe_2O_3$ at high pressures and temperatures, Nat. Commun. **7**, 10661 (2016).
[73] Yanming Ma, Artem R. Oganov, and Colin W. Glass, Structure of the metallic $\zeta$-phase of oxygen and isosymmetric nature of the $\varepsilon$-$\zeta$ phase transition: Ab initio simulations, Phys. Rev. B **76**, 064101 (2007).
[74] Cheng Lu, Maximilian Amsler, and Changfeng Chen, Unraveling the structure and bonding evolution of the newly discovered iron oxide $FeO_2$, Phys. Rev. B **98**, 054102 (2018).
[75] Russell Julian Hemley, Guido L. Chiarotti, and M. Bernasconi, *High Pressure Phenomena* (IOS Press, Amsterdam, 2002), Vol. 147.
[76] A. Grzechnik, L. Farina, R. Lauck, K. Syassen, I. Loa, and Pierre Bouvier, Pressure-induced structural deformations in $SeO_2$, J. Solid State Chem. **168**, 184 (2002).
[77] Denis Orosel, Olivier Leynaud, Paul Balog, and Martin Jansen, Pressure-temperature phase diagram of $SeO_2$. Characterization of new phases, J. Solid State Chem. **177**, 1631 (2004).
[78] Michele Ceriotti, Fabio Pietrucci, and Marco Bernasconi, Ab initio study of the vibrational properties of crystalline $TeO_2$: The $\alpha$, $\beta$, and $\gamma$ phases, Phys. Rev. B **73**, 104304 (2006).
[79] Matthias Weil, Redetermination of the $\gamma$-form of tellurium dioxide, IUCrData **2**, x171757 (2017).